NANO LETTERS
Letter
pubs.acs.org/NanoLett

Improving the Performance of Graphene Phototransistors Using a Heterostructure as the Light-Absorbing Layer

Xiaoqing Chen,[†,‡] Xiaolong Liu,[†,§] Bing Wu,[†] Haiyan Nan,[∥] Hui Guo,[‡] Zhenhua Ni,[∥] Fengqiu Wang,[†] Xiaomu Wang,[†] Yi Shi,*[,†] and Xinran Wang*[,†]

[†]National Laboratory of Solid State Microstructures, School of Electronic Science and Engineering, and Collaborative Innovation Center of Advanced Microstructures, Nanjing University, Nanjing 210093, China

[‡]School of Microelectronics, Xidian University, Xian 710071, China

[§]Beijing Key Laboratory of Novel Thin Film Solar Cells, Renewable Energy School, North China Electric Power University, Beijing 1002206, China

[∥]Department of Physics, Southeast University, Nanjing 211189, China

Supporting Information

ABSTRACT: Interfacing light-sensitive semiconductors with graphene can afford high-gain phototransistors by the multiplication effect of carriers in the semiconductor layer. So far, most devices consist of one semiconductor light-absorbing layer, where the lack of internal built-in field can strongly reduce the quantum efficiency and bandwidth. Here, we demonstrate a much improved graphene phototransistor performances using an epitaxial organic heterostructure composed of perylene-3,4,9,10-tetracarboxylic dianhydride (PTCDA) and pentacene as the light-absorbing layer. Compared with single light-absorbing material, the responsivity and response time can be simultaneously improved by 1 and 2 orders of magnitude over a broad band of 400−700 nm, under otherwise the same experimental conditions. As a result, the external quantum efficiency increases by over 800 times. Furthermore, the response time of the heterostructured phototransistor is highly gate-tunable down to sub-30 μs, which is among the fastest in the sensitized graphene phototransistors interfacing with electrically passive light-absorbing semiconductors. We show that the improvement is dominated by the efficient electron−hole pair dissociation due to interfacial built-in field rather than bulk absorption. The structure demonstrated here can be extended to many other organic and inorganic semiconductors, which opens new possibilities for high-performance graphene-based optoelectronics.

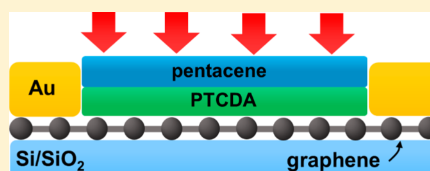

KEYWORDS: *Organic semiconductors, graphene, heterostructure, phototransistors, two-dimensional*

Graphene is a promising material for high-speed optoelectronics due to its broadband, tunable optical absorption and high carrier mobility.[1,2] However, graphene itself has low light absorption (∼2.3%) in the visible and near-infrared spectrum range.[3] To build high-responsivity photodetectors, an effective strategy is to interface graphene with light-sensitive semiconductors.[4,5] In these devices, the photoinduced electron−hole pairs are generated in the semiconductor, dissociated at the interface, and collected by graphene to give photocurrent. Various types of semiconductors have been used so far, such as quantum dots,[6] nanoplates,[7] transition-metal dichalcogenides,[8] organic small molecules/polymers,[9,10] and perovskites.[11] However, this type of devices naturally suffers from the photoresponsivity (R)−response time (τ) trade-off. The deep traps in the light-absorbing layer cause ultrahigh photoconductive gain (G) and R but at the same time sacrifice the operational bandwidth. In addition, most graphene-based hybrid phototransistors consist of only one semiconductor light-absorbing layer. The lack of internal electric field (within the light-absorbing layer) can prevent the efficient separation of electron−hole pairs and cause low quantum efficiency (QE). As a result, the devices have to rely on long intrinsic τ (typically in the range of milliseconds to seconds[10,12,13] without gate pulses) to achieve high R. Recently, several strategies using external field modulation have been put forward to remedy this trade-off. For example, the use of ferroelectric substrate[14] or top transparent electrode[15] can introduce a vertical field to increase the charge separation efficiency, while the ionic polymer gate can screen the charge traps and reduce the time response.[8] However, these approaches involve more complex device fabrication processes, and the best devices can only operate at sub-1 ms time scale.

Here, we report the simultaneous optimization of R, τ, and QE of graphene-based phototransistors by rational design of heterostructure as the light-absorbing layer. Instead of using the external gate field to facilitate charge separation, here we exploit the intrinsic built-in electric field at the semiconductor interfaces. Taking organic oligomers PTCDA and pentacene as an example, we show that the graphene/PTCDA/pentacene (GPP) phototransistors can achieve $R = 10^5$ A/W, intrinsic τ

Received: July 31, 2017
Revised: August 26, 2017
Published: September 6, 2017

ACS Publications © 2017 American Chemical Society

DOI: 10.1021/acs.nanolett.7b03263
Nano Lett. 2017, 17, 6391−6396

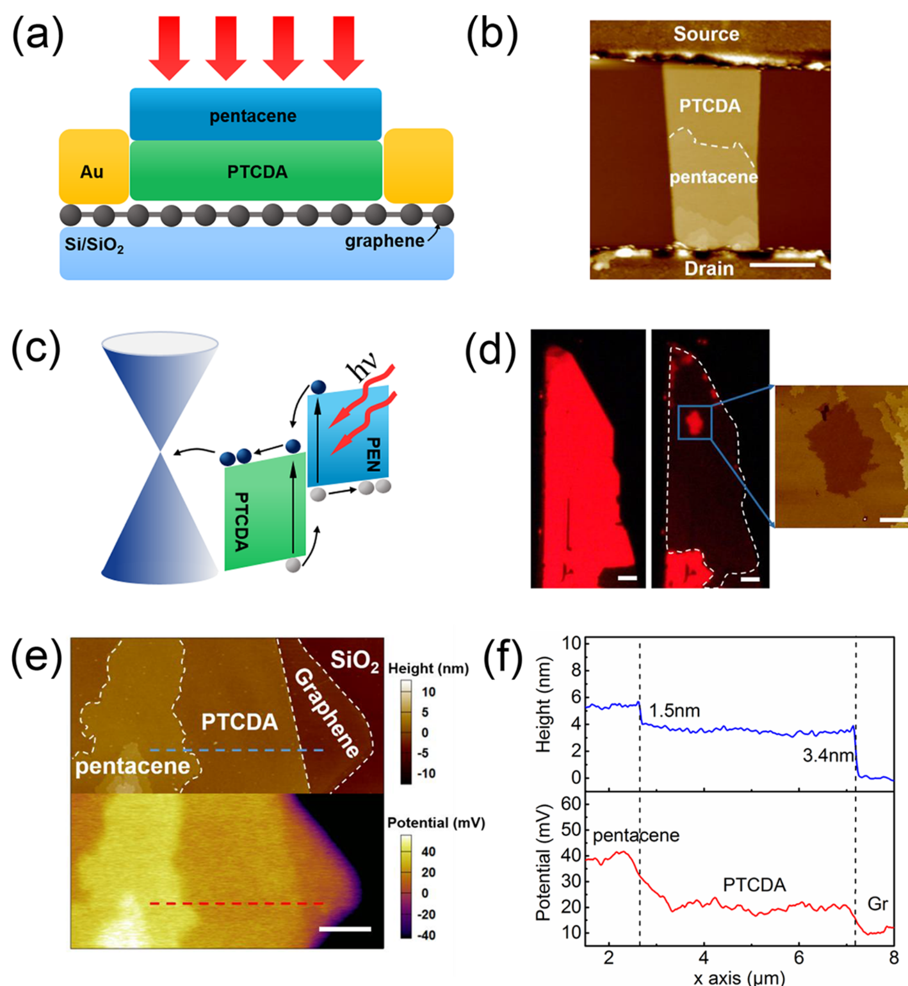

Figure 1. Schematics and operation principles of GPP phototransistors. (a) Schematic illustration and (b) AFM image of a GPP phototransistor structure. The device in panel b is fully covered by PTCDA and partially covered by pentacene for clarity. Scale bar, 2 μm. (c) Energy band diagram of the GPP phototransistor. (d) PL mapping of a *h*-BN/PTCDA sample before (left panel) and after pentacene growth (middle panel). Scale bars, 5 μm. The dashed line denotes the contour of the sample. The red region marked by the solid square was not covered by pentacene as shown in the AFM in the right panel, therefore showing bright PL. Scale bar, 2 μm. (e) AFM (top panel) and SKPM (lower panel) images of a graphene partially covered by PTCDA and pentacene. Scale bar, 2 μm. (f) Height and surface potential profiles along the dash lines in panel e. The height of the PTCDA is ~3.4 nm, corresponding to 11 layers. The height of each pentacene layer is ~1.5 nm. The built-in potential is stronger at PTCDA/pentacene than PTCDA/graphene interface.

down to 28 μs, and internal QE (IQE) up to 64%. Compared to graphene/PTCDA, R, τ, and QE all have huge improvement that are much beyond the combined absorption of each individual material. We find that the high-quality PTCDA/pentacene interface facilitates the formation of charge transfer (CT) states, which more effectively dissociates the electron–hole pairs generated in both materials and leads to much higher QE.

Following our previous works,[9] the GPP phototransistors were fabricated by van der Waals (vdW) epitaxy on graphene field-effect transistors (FETs) in a vacuum tube furnace (see Experimental Section for details of fabrication). To avoid any organic residue and preserve the clean surface of graphene, the Au electrodes were mechanically transferred onto graphene without lithography.[16] PTCDA has to grow first because it has higher evaporation temperature, therefore is stable during the subsequent pentacene growth. We performed atomic force microscopy (AFM) to obtain the topological information on each layer. Figure 1a and b shows the device schematics and AFM image of a typical GPP phototransistor (the pentacene does not cover the entire device for better clarity). Both PTCDA and pentacene are grown in a layer-by-layer fashion with ~0.3 nm and ~1.5 nm layer thickness, respectively (Figure 1f). The small height of the PTCDA layer suggests that it adopts the face-on packing as predicted theoretically and observed on epitaxial graphene.[17−19] The height of pentacene, on the other hand, is consistent with the thin-film phase, suggesting that is has the usual herringbone-type packing.[20] The PTCDA film often grows uniformly across the whole sample, while pentacene tends to nucleate near one electrode and extends to the other (Figure S1). The average thickness of PTCDA and pentacene ranges 4−20 nm and 1−3 nm in our GPP devices, respectively. Despite their distinct growth behavior, both materials are smooth and single-crystalline according to the cross-polarized optical micrographs (Figure S2), giving very high interface quality at both graphene/PTCDA and PTCDA/pentacene.

The combination of PTCDA and pentacene is chosen as the light-absorbing layer because of their complementary absorption spectrum in the visible range (Figure S3) as well as the

DOI: 10.1021/acs.nanolett.7b03263
Nano Lett. 2017, 17, 6391−6396

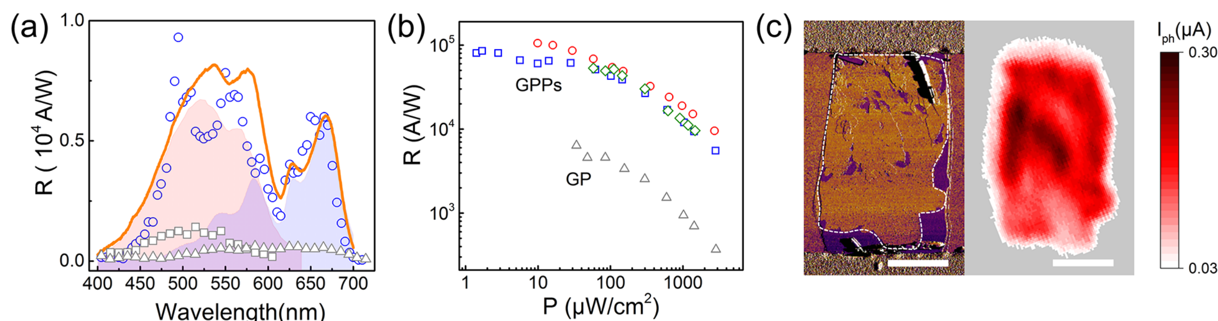

Figure 2. Photoresponse of GPP and control devices. (a) *R*-wavelength of a representative GPP device (blue circles, the average thickness of PTCDA/pentacene and coverage of pentacene is 4 nm/1.3*L*/82%) and control devices (gray squares: graphene/PTCDA; gray triangles: graphene/pentacene). The laser power is 100 μW for all the measurements. Red and blue shaded areas correspond to the absorption of PTCDA and pentacene. The summation of the two absorption spectra results in the yellow curve which well fits the GPP broadband photoresponse. (b) *R* as a function of laser power density for three GPP phototransistors and the graphene/PTCDA control device. The average thickness of PTCDA/pentacene and coverage of pentacene of GPPs is 11.3 nm/1.1*L*/71% (red circles), 12 nm/3*L*/93% (blue squares), and 19 nm/4.5*L*/94% (olive rhombus). The measurements in panels a and b were performed under V_{ds} = 0.1 V, $V_g - V_0 = -10$ V. (c) The left panel is the AFM phase image of a GPP device, with the heterostructure area outlined. The right panel is the photocurrent mapping of the device. Scale bars, 5 μm.

unique band alignment depicted in Figure 1c. Since PTCDA (pentacene) is a well-known n-type (p-type) oligomer with electron affinity (ionization energy) of 4.7 eV (5 eV), electron transfer from PTCDA to pentacene is expected upon contact, forming type-II heterojunction.[21,22] Furthermore, a weak electron transfer from graphene to PTCDA has been observed by photoemission spectroscopy.[23] The energy diagram in Figure 1c is consistent with these previous spectroscopic studies, where the vertical built-in field effectively separates the electron−hole pairs formed in both materials. Under light illumination electron−hole pairs are created in both PTCDA and pentacene, followed by the formation of a CT state at the PTCDA/pentacene interface. The electrons are collected by graphene and circulate while the holes reside in the pentacene layer which leads to the shift of Dirac point (Figure S4). To experimentally verify the constructed energy diagram of GPP, we carried out photoluminescence (PL) imaging and scanning Kelvin probe microscopy (SKPM). Figure 1d shows the PL image of PTCDA (left) and PTCDA/pentacene heterostructure (middle) grown on boron nitride substrate, under otherwise the same experimental conditions. We observed uniform and bright PL from the PTCDA layer, but the luminescence was quenched on the heterostructure (except the uncovered PTCDA area, Figure 1d, right panel), indicating strong charge transfer as expected for the type-II heterojunction. The band diagram is further corroborated by SKPM. Figure 1e shows the corresponding AFM and SKPM images of a graphene/11-layer PTCDA/few-layer pentacene sample. The surface potential is lowest and highest for pentacene and graphene, respectively, and only changes abruptly at the steps (Figure 1f). This confirms that the formation of interface dipoles and built-in electric field in the vertical direction as shown in Figure 1c.

Next, we performed photocurrent measurements on GPP phototransistors (see Methods for details of measurements). Compared with phototransistors with single light-absorbing material (PTCDA or pentacene), a typical GPP device shows ~10-fold improvement in *R* over a broad band of 400−700 nm (Figure 2a). The wavelength-dependent *R* can be nicely fit by summation of the absorption from PTCDA and pentacene, proving that the photoresponse is dominated by the oligomers. The *R* of GPP devices can reach 10^5 A/W under low light intensity, while the graphene/PTCDA control device has a maximum $R \sim 6.3 \times 10^3$ A/W, measurable only under much intense laser power (Figure 2b). The decrease of *R* at high incident power is consistent with other graphene phototransistors, which is due to the reduction of built-in field with a large number of photogenerated carriers.[6] The poor performance of the control devices is consistent with the weak charge transfer between graphene and PTCDA,[23] due to the relatively small energy misalignment. We note that all of the tests above were performed under negative V_g (p-doping). Under positive V_g, on the other hand, the GPP devices showed a smaller *R* and much faster τ, while the photoresponse of graphene/PTCDA control devices was almost undetectable (Figure S5). The *R*-wavelength for a GPP device in both electron and hole branches is plotted in Figure S6. We can see that the shape of the R spectrum does not change significantly with V_g. This suggests that the mechanism of GPP does not depend on the gate voltage, as expected. The large gate tunability will be discussed later. We further did high-resolution spatial photocurrent mapping on GPP phototransistors to characterize the influence of the heterostructure at microscopic scale (see Methods for details). Figure 2c shows the AFM phase image and photocurrent mapping result of a GPP device, where the area covered by pentacene is highlighted. The heterostructure region shows notable enhancement of photocurrent compared to bare PTCDA, consistent with single-point measurements.

To understand whether the enhancement of *R* originates from bulk absorption effects or interfacial effects, we performed thickness-dependent studies on the same GPP phototransistor subject to repeated pentacene growth (Figure S7). We found that *R* did not increase with the thickness of pentacene as long as a significant portion of the device area was covered by the heterostructure. In addition, the ratio of *R* at 500 nm (mainly by PTCDA) and 670 nm (mainly by pentacene) did not show strong dependence on the thickness of either material (Figure S8). Both evidence, together with the fact that the increase of *R* occurred in a broad band beyond the absorption of either material (Figure 2a), points to interfacial effects as the main reason behind the improved performance, similar to organic donor−acceptor systems.[24] We note that the shape of the *R*-wavelength varies from device to device (Figure 2a, Figures S7 and S9), which may depend on the detailed morphology and coverage of pentacene and PTCDA layers (Figure S9).

DOI: 10.1021/acs.nanolett.7b03263
Nano Lett. 2017, 17, 6391−6396

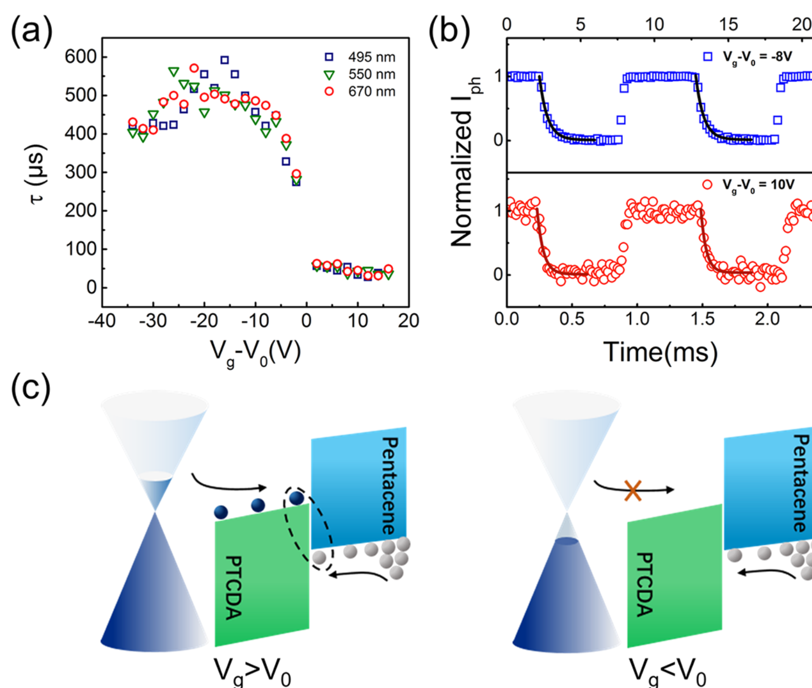

Figure 3. Dynamic response of GPP phototransistors. (a) τ−V_g relationship of the GPP device in Figure 2a. Blue squares, green triangles, and red circles represent 495, 550, and 670 nm laser illumination, respectively. (b) The dynamic response curves under 550 nm, $V_g - V_0 = -8$ V (top panel) and $V_g - V_0 = 10$ V (bottom panel). The solid lines are exponential fitting of the trailing edges. (c) The energy diagram of the recombination process for $V_g - V_0 > 0$ (left) and $V_g - V_0 < 0$ (right).

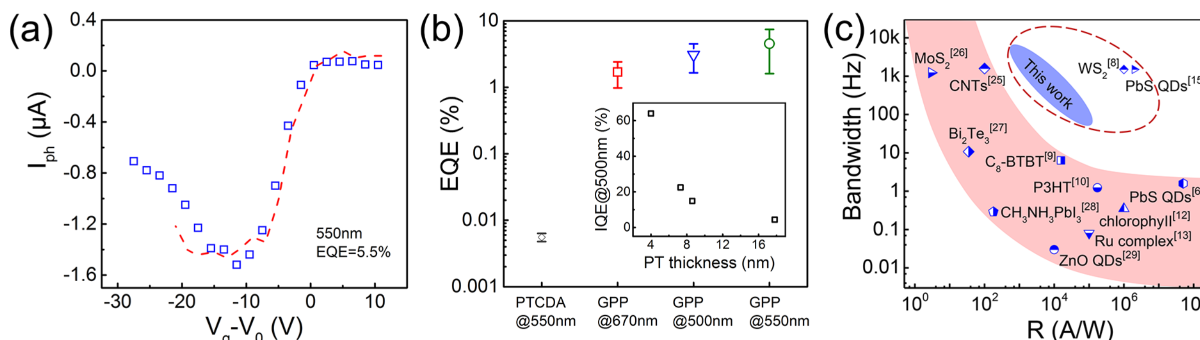

Figure 4. QE analysis. (a) The I_{ph}−V_g characteristics of a GPP phototransistor under 550 nm laser illumination (blue squares) together with a theoretical fit using experimentally derived parameters (red dashed line). From the fitting, EQE ∼ 5.5% is derived. (b) Statistical analysis of EQE of graphene/PTCDA devices at 550 nm and GPP devices at 670, 500, and 550 nm. The inset image is the IQE of GPP devices at 500 nm with different PTCDA thicknesses. For all devices, the laser power was as low as possible while maintaining good single-to-noise ratio. (c) Summary of device performance of sensitized graphene phototransistors with different semiconductors. Devices sensitized with single electrical passive light-absorbing layer are marked by the pink shadow. The red dashed line encircles the devices using vertical field. The blue region denotes GPP devices. The bandwidth is calculated by BW = $1/2\pi\tau$.

The dynamic response is another important aspect of phototransistors. The typical τ of PTCDA/graphene and pentacene/graphene phototransistors is hundreds and tens of milliseconds, respectively (Figure S10). Figure 3a shows the τ−V_g relationship of a representative GPP device (the same device as Figure 2a) under different laser wavelengths, obtained by exponential fitting of the photocurrent trailing edge (Figure 3b). Two different regimes are separated by $V_g = V_0$, which corresponds to the cross point between the transfer curves under dark and illumination (Figure S4a). In the hole branch ($V_g < V_0$), τ is on the order of several hundred μs, which is 2−3 orders of magnitude lower than the control devices. In the electron branch ($V_g > V_0$), τ is reduced by another order of magnitude to several tens of microseconds. Inside each regime, τ shows a weak V_g and wavelength dependence. According to the absorption spectra (Figure S3), PTCDA and pentacene absorbs mostly in 400−500 nm and 600−700 nm, respectively, while they both have absorption in 500−600 nm. The wavelength independence suggests that the response time does not depend on which material the electron−hole pairs are generated, as expected from Figure 1c. The τ−V_g can be explained by the energy diagrams in Figure 3c. When $V_g > V_0$, graphene has a high density of electrons, which can easily diffuse back into the hole-rich pentacene, resulting in a short lifetime. When $V_g < V_0$, on the other hand, graphene is also electron-deficient, so it takes a much longer time for electrons to neutralize holes on pentacene.

In the electron branch, the intrinsic response time in our GPP devices can be as low as 28 μs (Figure 3a), which is, to the best of our knowledge, the fastest graphene phototransistors

DOI: 10.1021/acs.nanolett.7b03263
Nano Lett. 2017, 17, 6391−6396

with electrically passive light-absorbing layers.[6,8−10,12,13,25−29] The τ is almost 4 orders of magnitude smaller than solution processed organic/graphene phototransistors[10,12,13] and 3 orders of magnitude smaller than our previously reported graphene/C_8-BTBT devices.[9] Considering the similar I_{ph} rising and falling times (Figure 3b, S11), we expect that the GPP phototransistors can operate at over 5 kHz bandwidth. The extraordinary response time in the GPP phototransistors is most likely due to three aspects. From AFM and cross-polarized microscopy (Figure S1 and S2), the PTCDA and pentacene are highly crystalline, and their interface is atomically smooth. This leads to a low density of charge traps in the GPP phototransistors. Furthermore, the local molecular arrangements may facilitate charge transfer at the two interfaces. We speculate this may be the main reason that GPP is much faster than the graphene/C8-BTBT devices.[9] Finally, the large I_{ph} generates a high density of mobile charges on graphene, which could saturate the traps in the substrate[8] and lead to a fast response time.

In a sensitized graphene phototransistor,

$$R = \frac{q}{E_{ph}} \times G \times \text{EQE} = \frac{q}{E_{ph}} \frac{\tau}{\tau_{transit}} \times \text{EQE} \quad (1)$$

where q is the elementary charge, E_{ph} is the photon energy, $\tau_{transit} = L^2/(\mu V_{ds})$ is the carrier transit time across the graphene channel with length of L, and μ is the carrier mobility. Since all of the parameters in eq 1 are directly measurable except EQE, we can derive it as[15]

$$\text{EQE} = \frac{E_{ph}}{q} \times R \times \frac{\tau_{transit}}{\tau} \quad (2)$$

Figure 4a plots the I_{ph}−V_g of a GPP phototransistor under 550 nm illumination, together with theoretical fit using experimentally measured R, μ, and τ. The fitting was excellent over the entire V_g range, showing a constant EQE of 5.5% without gain. Among all fabricated GPP devices, the maximum EQE is 9% at 550 nm, 4.9% at 500 nm, and 2.7% at 670 nm, while the maximum EQE of graphene/PTCDA is 0.006% at 550 nm (Figure 4b). The latter is comparable to other reported graphene/organic phototransistors.[12] Compared with graphene/PTCDA, the average EQE of GPP is boosted by ~800 times at 550nm from the statistical results in Figure 4b. We can further calculate the IQE = EQE/η_{abs}, where η_{abs} is the absorption of the incident photons by PTCDA and pentacene. Since the PTCDA is very uniform with precisely measured thickness, we can estimate the IQE at 500 nm (where PTCDA is the dominant absorber) using the well-documented extinction coefficient in the literature.[30] We find that the IQE has a strong dependence on PTCDA thickness, decreasing from 64% at 4 nm to 4.4% at 17.8 nm (Figure 4b, inset). The highest IQE of 64% is comparable to the best inorganic quantum dots/graphene hybrid phototransistors and MoS_2/graphene vertical photodetectors.[6,15,31] The strong thickness dependence of IQE suggests that PTCDA far away from the interface plays only minor roles in charge separation, which reaffirms that interfacial mechanism is responsible for the performance improvement. On the basis of these arguments, we can estimate the depletion width of the junction to be only a few nanometers. Finally, the performance of sensitized graphene phototransistors with different light-absorbing materials is summarized in Figure 4c, showing a clear trade-off between bandwidth and responsivity by the nature of this type of devices. Due to the simultaneously improvement in R and τ, the GPP devices lie in the top right corner of the diagram, showing the best overall performance so far. From Figure 4c, all of the sensitized graphene phototransistors thus far suffer from low bandwidth below 10 kHz. However, the intrinsic bandwidth is limited by the charge transfer process between a semiconductor and graphene, which could be on the order of subpicosecond.[32] Therefore, all of the sensitized phototransistors are still limited by extrinsic factors. The key to further improve bandwidth is to design proper interface and remove charge traps in the device as much as possible.

In conclusion, we demonstrate the use of heterostructure as the light-absorbing layer to greatly enhance the performance of graphene-based phototransistors. Compared with individual light-absorbing semiconductors, the GPP heterostructure significantly improves R, τ, and QE at the same time. The performance improvement is due to the built-in field in the heterostrcuture which effectively separates the generated electron−hole pairs. We would like to point out that the PTCDA/pentacene combination is just one example of this concept. There are many other combinations of organic and inorganic semiconductors that fulfill similar band alignment. Furthermore, we expect that energy diagram with reverse built-in field would also work the same way by choosing appropriate materials (Figure S12).

Methods. *GPP Device Fabrication and Characterization.* We first fabricated backgated graphene field-effect transistors on 300 nm SiO_2/Si substraste with Au electrode.[9] The transistors were placed in a tube furnace to grow PTCDA and pentacene sequentially. Specifically, PTCDA (purchased from Sigma-Aldrich with a purity of 97% without further purification) and pentacene (purchased from TCI with a purity of 99% without further purification) powder were placed at the center of the furnace, and the graphene FETs were located downstream. The growth temperatures for PTCDA and pentacene were 230 and 120 °C, respectively, under 1×10^{-4} Torr vacuum. AFM and SKPM characterizations were performed by an Asylum Research Cypher system in ambient atmosphere. Conductive tips (Multi75E-G) coated with Cr/Pt biased at +3 V were used for SKPM. Under such condition, the material with a lower surface potential exhibits relatively smaller potential difference with the biased tip and shows up as a brighter color. Photoluminescence mapping was performed at 450 nm LED illumination, and PL signal is collected by a CCD equipped with a 500 nm high-pass filter.

Photocurrent Measurements. The spectral response measurement was done with a supercontinuum white-light laser source (Fianium WhiteLase SC400) in a close-cycle cryogenic vacuum probe station. The laser was collimated to a uniform 3 mm spot through an aperture. Photocurrents were detected by Keithley 4200 SMU modules, and Agilent 4156C was used to output V_g. Time-resolved measurements were done by Keithley 4200 PMU and a mechanical chopper placed on the laser path. The photocurrent mapping was obtained by scanning over the device using Thorlabs GVS212 and modulated photocurrent signals were amplified and detected using lock-in (Stanford SR830) technique. Photocurrent mapping was performed under 637 nm laser illumination which was modulated by a square-wave signal generator source.

DOI: 10.1021/acs.nanolett.7b03263
Nano Lett. 2017, 17, 6391−6396

■ ASSOCIATED CONTENT

Supporting Information

The Supporting Information is available free of charge on the ACS Publications website at DOI: 10.1021/acs.nanolett.7b03263.

Additional information and details on growth, characterization of devices, and device performance (PDF)

■ AUTHOR INFORMATION

Corresponding Authors

*E-mail: xrwang@nju.edu.cn.
*E-mail: yshi@nju.edu.cn.

ORCID

Bing Wu: 0000-0003-4302-1875
Zhenhua Ni: 0000-0002-6316-2256
Xinran Wang: 0000-0002-3975-1667

Author Contributions

X.C. and X.L. contributed equally. X.R.W. and Y.S. conceived and supervised the project. X.C., X.L., B.W., and H.N. performed experiments and data analysis. H.G., Z.N., X.M.W., and F.W. contributed to data analysis. X.R.W., X.L., and X.C. cowrote the paper. All authors discussed the results and commented on the manuscript.

Notes

The authors declare no competing financial interest.

■ ACKNOWLEDGMENTS

This work was supported in part by National Natural Science Foundation of China 61325020, 61521001, 61106079, 61575153; National Key Basic Research Program of China 2013CBA01604 and 2015CB351900; "Jiangsu Shuangchuang" program and "Jiangsu Shuangchuang Team" Program, Key Laboratory of Advanced Photonic and Electronic Materials, Collaborative Innovation Center of Solid-State Lighting and Energy-Saving Electronics, and the Fundamental Research Funds for the Central Universities, China.

■ REFERENCES

(1) Bonaccorso, F.; Sun, Z.; Hasan, T.; Ferrari, A. C. *Nat. Photonics* **2010**, *4*, 611−622.
(2) Xia, F.; Wang, H.; Xiao, D.; Dubey, M.; Ramasubramaniam, A. *Nat. Photonics* **2014**, *8*, 899−907.
(3) Nair, R. R.; Blake, P.; Grigorenko, A. N.; Novoselov, K. S.; Booth, T. J.; Stauber, T.; Peres, N. M. R.; Geim, A. K. *Science* **2008**, *320*, 1308−1308.
(4) Zhao, H.; Guo, Q.; Xia, F.; Wang, H. *Nanophotonics* **2015**, *4*, 128−142.
(5) Liu, Y.; Weiss, N. O.; Duan, X.; Cheng, H.-C.; Huang, Y.; Duan, X. F. *Nat. Rev. Mater.* **2016**, *1*, 16042.
(6) Konstantatos, G.; Badioli, M.; Gaudreau, L.; Osmond, J.; Bernechea, M.; de Arquer, F. P. G.; Gatti, F.; Koppens, F. H. L. *Nat. Nanotechnol.* **2012**, *7*, 363−368.
(7) Wang, Q. S.; Wen, Y.; He, P.; Yin, L.; Wang, Z. X.; Wang, F.; Xu, K.; Huang, Y.; Wang, F. M.; Jiang, C.; He, J. *Adv. Mater.* **2016**, *28*, 6497.
(8) Mehew, J. D.; Unal, S.; Torres Alonso, E.; Jones, G. F.; Fadhil Ramadhan, S. F.; Craciun, M. F.; Russo, S. *Adv. Mater.* **2017**, *29*, 1700222.
(9) Liu, X.; Luo, X.; Nan, H.; Guo, H.; Wang, P.; Zhang, L. L.; Zhou, M. M.; Yang, Z. Y.; Shi, Y.; Hu, W. D. *Adv. Mater.* **2016**, *28*, 5200−5205.
(10) Huisman, E. H.; Shulga, A. G.; Zomer, P. J.; Tombros, N.; Bartesaghi, D.; Bisri, S. Z.; Loi, M. A.; Koster, L. J. A.; van Wees, B. J. *ACS Appl. Mater. Interfaces* **2015**, *7*, 11083−11088.
(11) Wang, Y.; Zhang, Y.; Lu, Y.; Xu, W.; Mu, H.; Chen, C.; Qiao, H.; Song, J.; Li, S.; Sun, B. *Adv. Opt. Mater.* **2015**, *3*, 1389−1396.
(12) Chen, S. Y.; Lu, Y. Y.; Shih, F. Y.; Ho, P.-H.; Chen, Y. F.; Chen, C. W.; Chen, Y. T.; Wang, W. H. *Carbon* **2013**, *63*, 23−29.
(13) Liu, X.; Lee, E. K.; Oh, J. H. *Small* **2014**, *10*, 3700−3706.
(14) Tan, W.-C.; Shih, W.-H.; Chen, Y. F. *Adv. Funct. Mater.* **2014**, *24*, 6818−6825.
(15) Nikitskiy, I.; Goossens, S.; Kufer, D.; Lasanta, T.; Navickaite, G.; Koppens, F. H. L.; Konstantatos, G. *Nat. Commun.* **2016**, *7*, 11954.
(16) He, D.; Zhang, Y.; Wu, Q.; Xu, R.; Nan, H.; Liu, J.; Yao, J.; Wang, Z.; Yuan, S.; Li, Y. *Nat. Commun.* **2014**, *5*, 5162.
(17) Wu, B.; Zhao, Y.; Nan, H.; Yang, Z.; Zhang, Y.; Zhao, H.; He, D.; Jiang, Z.; Liu, X.; Li, Y. *Nano Lett.* **2016**, *16*, 3754−3759.
(18) Wang, Q. H.; Hersam, M. C. *Nat. Chem.* **2009**, *1*, 206−211.
(19) Zhao, Y.; Wang, J. *J. Phys. Chem. C* **2017**, *121*, 4488−4495.
(20) Zhang, Y.; Qiao, J.; Gao, S.; Hu, F.; He, D.; Wu, B.; Yang, Z.; Xu, B.; Li, Y.; Shi, Y. *Phys. Rev. Lett.* **2016**, *116*, 016602.
(21) Kahn, A.; Koch, N.; Gao, W. *J. Polym. Sci., Part B: Polym. Phys.* **2003**, *41*, 2529−2548.
(22) Koch, N.; Kahn, A.; Ghijsen, J.; Pireaux, J.-J.; Schwartz, J.; Johnson, R. L.; Elschner, A. *Appl. Phys. Lett.* **2003**, *82*, 70−72.
(23) Huang, H.; Chen, S.; Gao, X.; Chen, W.; Wee, A. T. S. *ACS Nano* **2009**, *3*, 3431−3436.
(24) Wang, T.; Zhao, C.; Zhang, L.; Lu, T.; Sun, H.; Bridgmohan, C. N.; Weerasinghe, K. C.; Liu, D.; Hu, W.; Li, W. *J. Phys. Chem. C* **2016**, *120*, 25263−25275.
(25) Liu, Y.; Wang, F.; Wang, X.; Wang, X. Z.; Flahaut, E.; Liu, X.; Li, Y.; Wang, X. W.; Xu, Y.; Shi, Y. *Nat. Commun.* **2015**, *6*, 8589.
(26) Li, X.; Wu, J.; Mao, N.; Zhang, J.; Lei, Z.; Liu, Z.; Xu, H. *Carbon* **2015**, *92*, 126−132.
(27) Qiao, H.; Yuan, J.; Xu, Z.; Chen, C.; Lin, S.; Wang, Y.; Song, J. C.; Liu, Y.; Khan, Q.; Hoh, H. Y. *ACS Nano* **2015**, *9*, 1886−1894.
(28) Lee, Y.; Kwon, J.; Hwang, E.; Ra, C.-H.; Yoo, W. J.; Ahn, J.-H.; Park, J. H.; Cho, J. H. *Adv. Mater.* **2015**, *27*, 41−46.
(29) Guo, W.; Xu, S.; Wu, Z.; Wang, N.; Loy, M. M. T.; Du, S. *Small* **2013**, *9*, 3031−3036.
(30) Vragović, I.; Scholz, R. *Phys. Rev. B: Condens. Matter Mater. Phys.* **2003**, *68*, 155202.
(31) Yu, W. J.; Liu, Y.; Zhou, H.; Yin, A.; Li, Z.; Huang, Y.; Duan, X. *Nat. Nanotechnol.* **2013**, *8*, 952−958.
(32) Long, R.; English, N. J.; Prezhdo, O. V. *J. Am. Chem. Soc.* **2012**, *134*, 14238−14248.

DOI: 10.1021/acs.nanolett.7b03263
Nano Lett. 2017, 17, 6391−6396